Electronic Supplementary Information (ESI) for

Electronic regulation of single-atomic Ti sites on metal hydroxide for boosting photocatalytic CO_2 reduction

Ning-Yu Huang,‡[a] Bai Li,‡[c] Duojie Wu,[d] Di Chen,[a] Yu-Tao Zheng,[a] Bing Shao,[a] Wenjuan Wang,[a] Meng Gu,[d] Lei Li*[c] and Qiang Xu*[a,b]

[a] Shenzhen Key Laboratory of Micro/Nano-Porous Functional Materials (SKLPM), SUSTech-Kyoto University Advanced Energy Materials Joint Innovation Laboratory (SKAEM-JIL), Department of Chemistry and Department of Materials Science and Engineering, Southern University of Science and Technology, Shenzhen 518055, China.

[b] Institute for Integrated Cell-Material Sciences (WPI-iCeMS), Kyoto University, Yoshida, Sakyo-ku, Kyoto 606-8501, Japan.

[c] Shenzhen Key Laboratory of Micro/Nano-Porous Functional Materials (SKLPM) and Department of Materials Science and Engineering, Southern University of Science and Technology, Shenzhen 518055, China.

[d] Department of Materials Science and Engineering and Guangdong Provincial Key Laboratory of Energy Materials for Electric Power, Southern University of Science and Technology, Shenzhen 518055, China

[‡] These authors contributed equally to this work.

*Corresponding authors: lil33@sustech.edu.cn, xuq@sustech.edu.cn, xu.qiang@icems.kyoto-u.ac.jp

Table of Contents

Table S3 Comparison of the photocatalytic activities of $Ti_1/Ni(OH)_2$ and other reported catalysts for photocatalytic CO_2 reduction to CO.

Experimental section

Chemicals and Materials. All reagents were commercially available and used without further purification. Nickel(II) nitrate hexahydrate ($Ni(NO_3)_2 \cdot 6H_2O$, ≥ 98%), *N*,*N*-dimethylformamide (DMF, ≥ 99.9%), Acetonitrile (CH_3CN, ≥ 99.9%), titanium diisopropoxide bis(acetylacetonate) (75 wt% in isopropanol) and isopropanol (≥ 99.5%) were purchased from Shanghai Aladdin Biochemical Technology Co., Ltd. Urea (≥ 99.0%) and ethanol (C_2H_5OH, ≥ 99.7%) were purchased from Shanghai Lingfeng Chemical Reagent Co., Ltd. $Ru(phen)_3Cl_2 \cdot H_2O$ (phen = 1,10-phenanthroline, ≥ 98%) and 1,3-dimethyl-2-phenyl-2,3-dihydro-1*H*-benzo[*d*]imidazole (BIH, ≥ 97%) were purchased from Bide Pharmatech Co., Ltd. Isopropanol (≥ 99.0%) was purchased from Shanghai Macklin Biochemical Co., Ltd.

Structural and morphological characterizations. Powder X-ray diffraction (PXRD) patterns were collected on a Rigaku SmartLab 9KW diffractometer with Cu Kα radiation. X-ray photoelectron spectroscopy (XPS) measurements were performed with a Thermo Fisher ESCALAB Xi+ instrument. Scanning electron microscope (SEM) images were obtained from Hitachi Regulus 8100 apparatus with an acceleration voltage of 10 kV. High-angle annular dark-field scanning transmission electron microscopy (HAADF-STEM) images were captured on Titan Cubed Themis G2 300 with a Bruker Quantax Super-X EDS detector. Silicon-contained contaminations from TEM specimens can be removed using plasma cleaner.[1] The X-ray absorption spectroscopy (XAS) data were collected at the BL-11B beamlines in the Shanghai Synchrotron Radiation Facility (SSRF) (Shanghai, China). UV-vis spectra were collected on a Shimadzu UV-3600i Plus instrument. Photoluminescence measurements were carried out on the HORIBA FluoroMax Plus R928P spectrofluorometer. The Mott-Schottky, photocurrent and electrochemical impedance spectroscopy (EIS) measurements were carried out on a CHI660e electrochemical workstation in 0.5 M Na_2SO_4 electrolyte with standard three electrode system, in which fluorine-doped tin oxide (FTO) glass, Ag/AgCl electrode and graphite rod was used as working electrode, reference electrode and counter electrode, respectively. The EIS measurement was performed at –0.5 V vs. Ag/AgCl over a frequency range from 0.1 Hz to 1.0 MHz with an AC voltage amplitude of 10 mV.

Synthesis of $Ni(OH)_2$. $Ni(OH)_2$ was synthesized via a typical hydrothermal reaction.[2] A mixture of $Ni(NO_3)_2 \cdot 6H_2O$ (1.05 g), urea (217.5 mg) and 60 mL distilled H_2O was mixed and sealed in a 100-mL Teflon vial. The vial was heated at 200 ℃ for 20 h. After cooling to room temperature, green powders were collected by centrifugation, washed with H_2O and C_2H_5OH, and then dried under vacuum at 60 ℃.

Synthesis of d-$Ni(OH)_2$. The as-synthesized $Ni(OH)_2$ (50.0 mg) was dispersed in a mixture of 4 mL DMF, 1.5 mL H_2O and 1.5 mL ethanol. After ultrasonication for 15 min, the mixture was sealed in a 25-mL Teflon vial and heated at 140 ℃ for 8 h. After cooling down to room temperature, green powders were collected by centrifugation, washed with DMF and C_2H_5OH, and then dried under vacuum at 60 ℃.

Synthesis of $Ti_1/Ni(OH)_2$. 50.0 mg of d-$Ni(OH)_2$ was dispersed in 1 mL isopropanol, followed by

the addition of 1 mL titanium diisopropoxide bis(acetylacetonate). The mixture was stirred under room temperature for 12 h and collected by centrifugation. After washing with ethanol for three time, the resulting powders were dried under vacuum at 60 °C and denoted as $Ti_1/Ni(OH)_2$.

Synthesis of $Zr_1/Ni(OH)_2$ and **$Hf_1/Ni(OH)_2$**. The synthesis process of $Zr_1/Ni(OH)_2$ and $Hf_1/Ni(OH)_2$ are similar to that of $Ti_1/Ni(OH)_2$, except that 0.1 M $ZrCl_4$ and 0.1 M $HfCl_4$ was used to replace titanium diisopropoxide bis(acetylacetonate).

XAFS data analysis. Acquired EXAFS data were processed according to standard procedures using the ATHENA module implemented in the IFEFFIT software packages. We obtained the EXAFS spectra through post-edge background subtraction from the overall absorption and normalizing with respect to the edge-jump step. The Ti *K*-edge k^2-weighted $\chi(k)$ data in the *k*-space ranging from 3 to 12 $Å^{-1}$ were Fourier-transformed to real (*R*) space using a Hanning windows (dk = 0.3 $Å^{-1}$) to separate the EXAFS contributions from different coordination shells. *R* represents the radial distribution function. To obtain the detailed structural parameters around the Ti atom in the as-prepared samples, quantitative curve fittings were carried out for the Fourier-transformed $k^2\chi(k)$ in *R*-space using the ARTEMIS module of IFEFFIT. Effective backscattering amplitudes $F(k)$ and phase shifts $\Phi(k)$ of all fitting paths were calculated with the ab initio code FEFF9.0. For the samples, a *k*-range of 3-12 $Å^{-1}$ was used and curve fittings were carried out in *R*-space within an *R* range of [1-2] Å for k^2-weighted $\chi(k)$ functions.

Photocatalytic Measurements. To prepare a colloidal suspension, 5 mg of catalysts were dispersed in 5 mL distilled H_2O with ultrasonication, and the amount of catalyst added in the photocatalytic system was determined by the volume of the suspension. The photocatalytic CO_2 reduction experiments were carried out under 1 atm CO_2 atmosphere in a 60-mL quartz reactor containing catalyst (1 mg), $Ru(phen)_3Cl_2$ (10 mg) BIH (40 mg) and the mixed solvent CH_3CN/H_2O (*v*/*v* = 4:1, 5 mL). The reaction mixture was continuously stirred and irradiated under LED light (400 – 800 nm) in a multi-channel photochemical reactiong system (PCX-50C, Beijing Perfectlight Co. Ltd., China). The reaction temperature was controlled as 25 °C by circulating water. The generated gas samples were analyzed by a GC-2014 gas chromatographer equipped with a thermal conductivity detector (TCD) and a flame ionization detector (FID). The liquid-phase were analyzed by a Bruker AVANCE III 400 MHz instrument. After a cycle of photocatalytic reduction, the catalyst was centrifuged and washed with water for the next run. After adding identical amount of fresh CH_3CN/H_2O, BIH and $[Ru(phen)_3]Cl_2·6H_2O$, CO_2 was reintroduced to the photocatalytic system under the same operating conditions. In isotope experiments, $^{13}CO_2$ was used to replace $^{12}CO_2$ as carbon source and the gas products were analyzed by gas chromatography-mass spectrometry (GC-MS, Agilent 7890B-5977A).

Density functional theory (DFT) calculations. All DFT calculations were performed using the projector augmented wave (PAW) method[3] with the plane-wave basis set as implemented in Vienna ab

initio simulation package (VASP) with a cutoff energy of 460 eV.[4] A cutoff energy of 460 eV was used. The Perdew-Burke-Ernzerhof (PBE) functional as formulated in the generalized gradient approximation (GGA)[5] was utilized to describe electronic exchange and correlation, and the projector augmented wave (PAW) method[3] was applied to represent the core-valence electron interaction. Hubbard U corrections (DFT+U) with U=5.5 for Ni 3*d* and U=3.5 for Ti 3*d* electrons were applied to mitigate the self-interaction error according to previous studies.[6] A gamma grid of 3 × 3 × 1 k-point was employed for all calculations. The convergence criterion for the electronic self-consistent filed loop was set to 1×10^{-5} eV. The structures were optimized until the residual forces of each atom were below 0.03 eV/Å. The β-$Ni(OH)_2$ (001) surface was modeled using a 3 × 3 periodically slab. For all surface systems, the bottom two-layer atoms were fixed to maintain the bulk structure while other atoms were fully relaxed (as shown in Figure S14d). A 15 Å vacuum space was used to minimize interaction from neighboring cells. The d-$Ni(OH)_2$ and $Ti_1/Ni(OH)_2$ were obtained by removing one Ni atom and replacing one Ni atom with a Ti atom from the first layer of β-$Ni(OH)_2$, respectively.

For CO_2 reduction to CO, following primary elemental steps are considered here:

$$CO_2 + * \rightarrow CO_2^* \quad (1)$$

$$CO_2^* + H^+ + e^- \rightarrow COOH^* \quad (2)$$

$$COOH^* + H^+ + e^- \rightarrow CO^* + H_2O \quad (3)$$

$$CO^* \rightarrow CO_{(g)} + * \quad (4)$$

The computational hydrogen electrode (CHE) model[7] was used to represent the chemical potentials of proton-electron pair. The Gibbs free energy changes (ΔG) for each element step was calculated by ΔG=ΔE+ΔZPE-TΔS, where the ΔE, ΔZPE and ΔS are the change of total energy, zero-point energy and entropy (298.15 K), respectively.

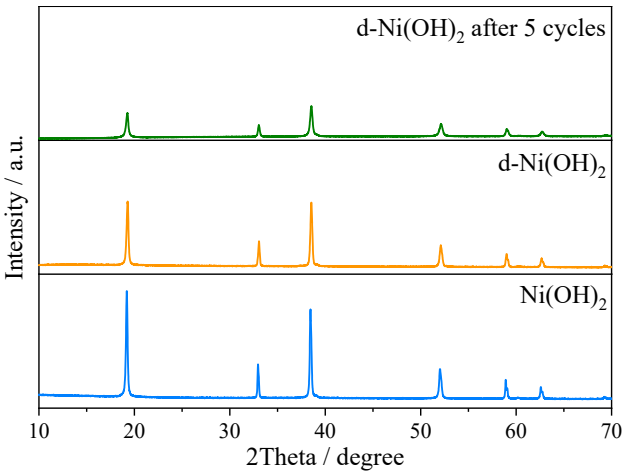

Fig. S1. PXRD patterns of $Ni(OH)_2$, d-$Ni(OH)_2$ and d-$Ni(OH)_2$ synthesized after 5 cycles.

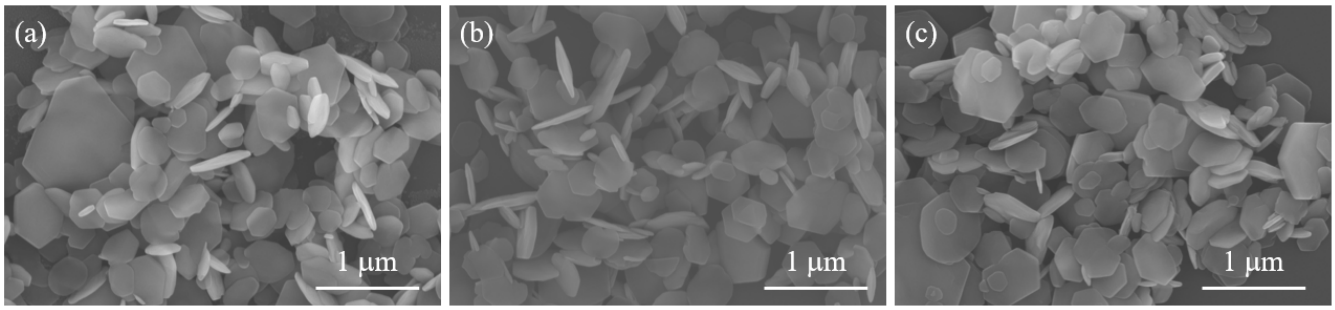

Fig. S2. SEM images of (a) $Ni(OH)_2$, (b) d-$Ni(OH)_2$ and (c) $Ti_1/Ni(OH)_2$.

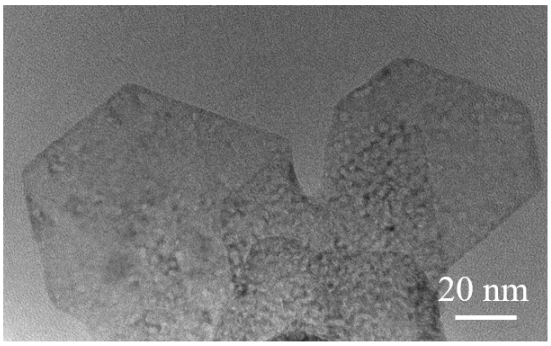

Fig. S3. TEM images of d-$Ni(OH)_2$.

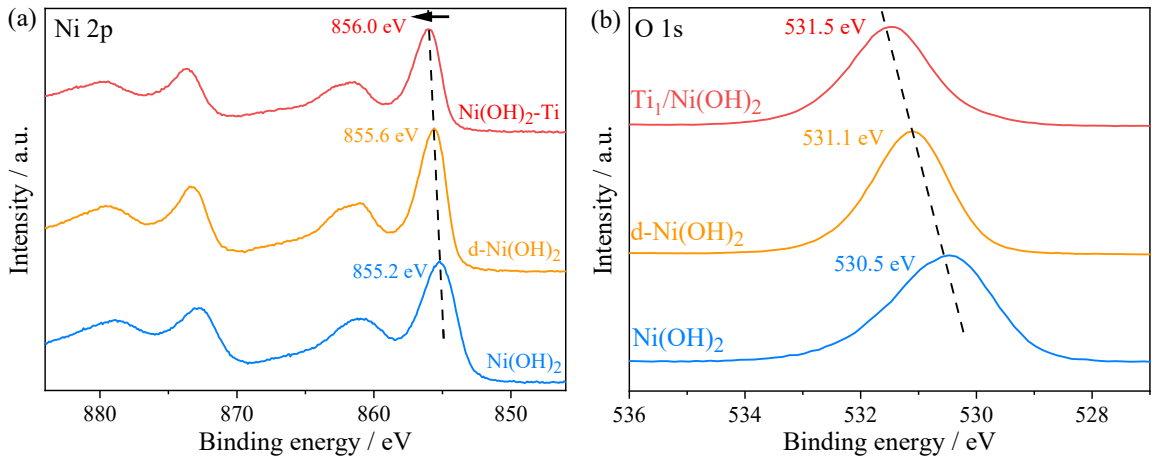

Fig. S4. (a) Ni 2p and (b) O 1s XPS spectra of $Ni(OH)_2$, d-$Ni(OH)_2$ and $Ti_1/Ni(OH)_2$.

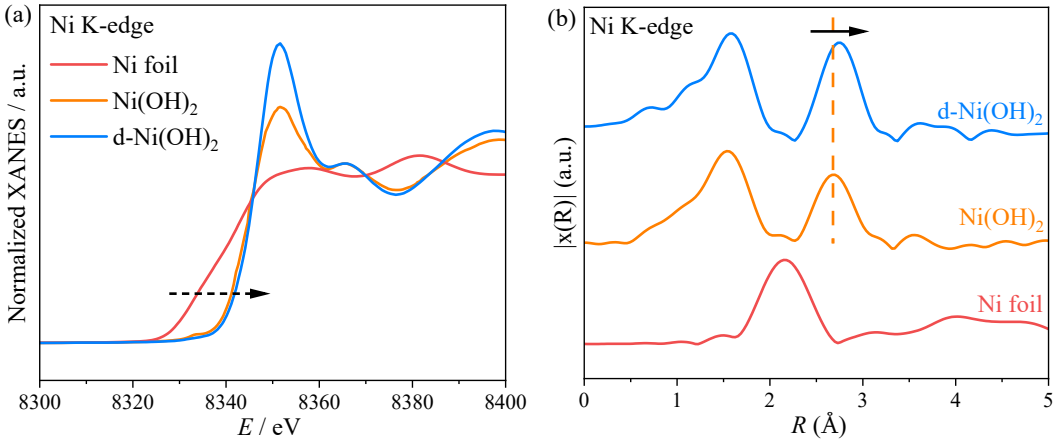

Fig. S5. Ni *K*-edge (a) XANES and (b) EXAFS spectra of d-$Ni(OH)_2$, $Ni(OH)_2$ and Ni foil.

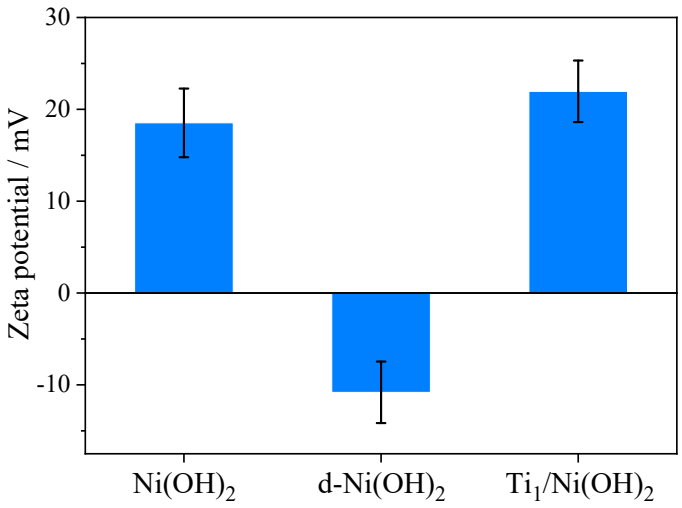

Fig. S6. Zeta potentials of $Ni(OH)_2$, d-$Ni(OH)_2$ and $Ti_1/Ni(OH)_2$.

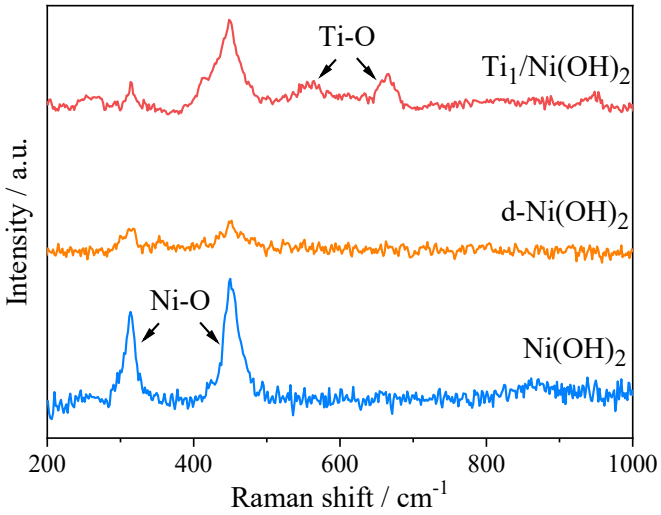

Fig. S7. Raman spectra of $Ti_1/Ni(OH)_2$, d-$Ni(OH)_2$ and $Ni(OH)_2$.

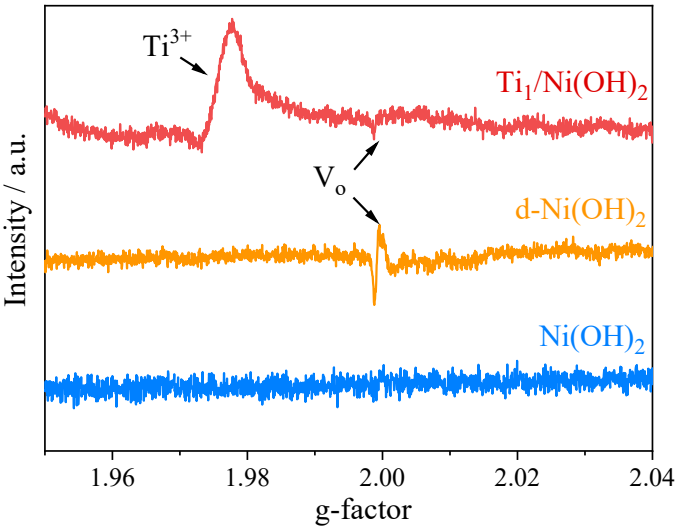

Fig. S8. EPR spectra of $Ni(OH)_2$, d-$Ni(OH)_2$ and $Ti_1/Ni(OH)_2$.

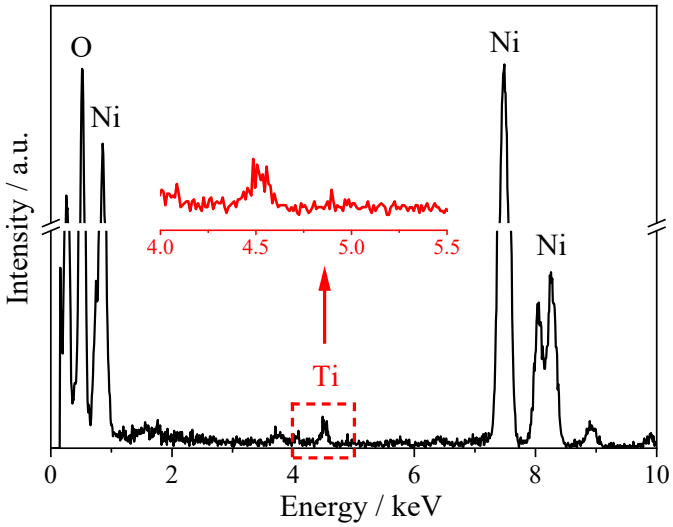

Fig. S9. EDS spectra of $Ti_1/Ni(OH)_2$.

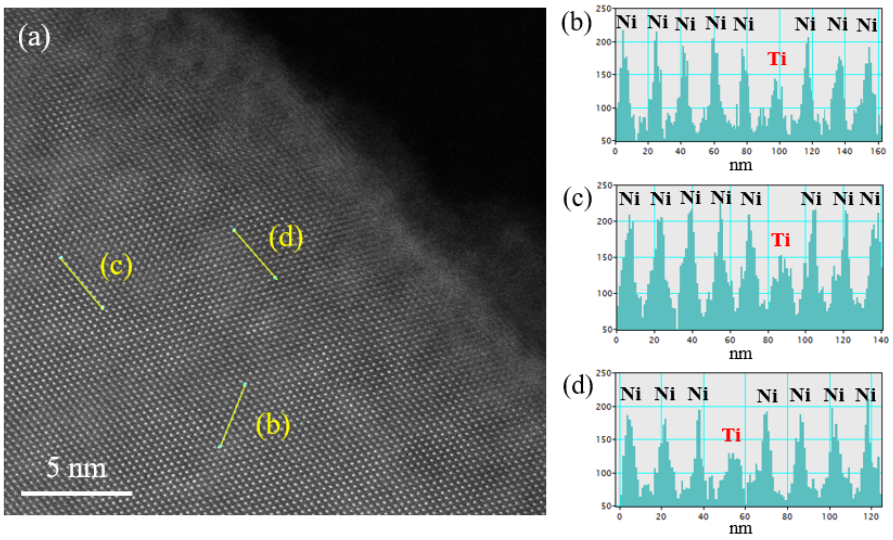

Fig. S10. (a) HAADF-STEM image of $Ti_1/Ni(OH)_2$ and (b-d) the corresponding brightness intensity of the yellow line profiles taken in the HAADF-STEM image.

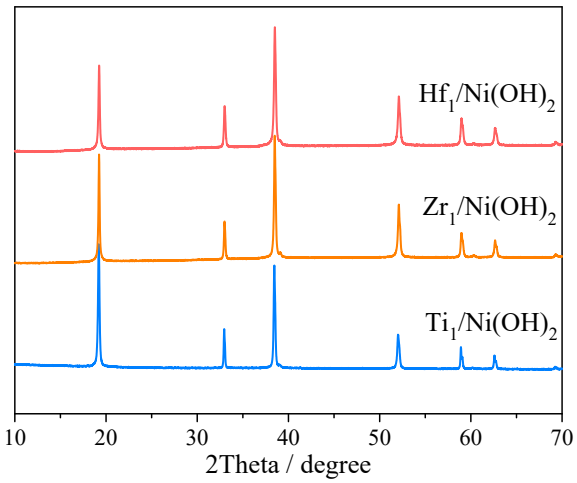

Fig. S11. PXRD patterns of $Ti_1/Ni(OH)_2$, $Zr_1/Ni(OH)_2$ and $Hf_1/Ni(OH)_2$.

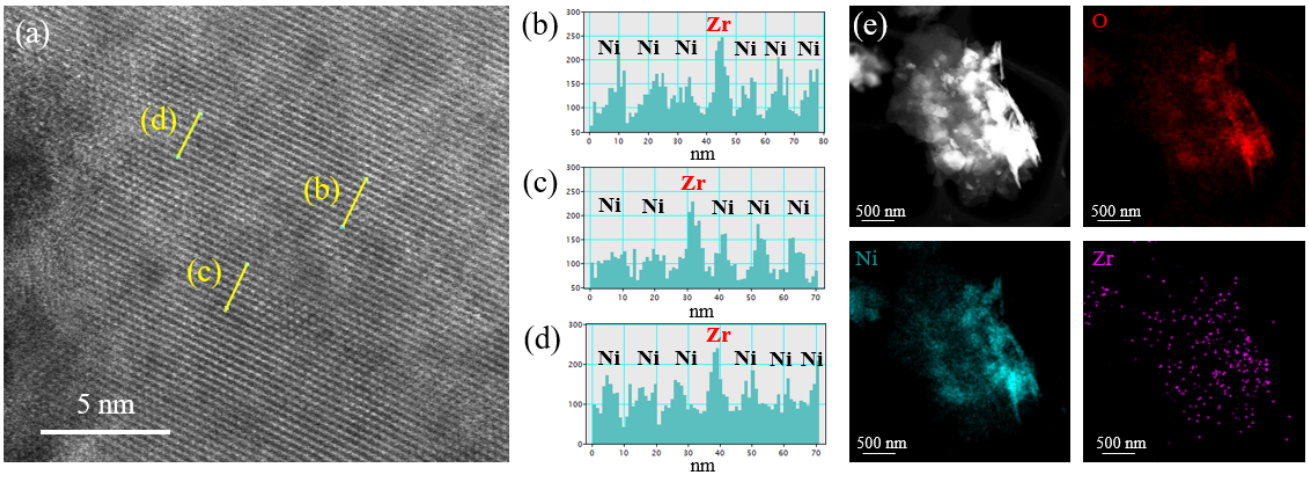

Fig. S12. (a) HAADF-STEM image of $Zr_1/Ni(OH)_2$ and (b-d) the corresponding brightness intensity of the yellow line profiles taken in the HAADF-STEM image. (e) HAADF-STEM image of $Zr_1/Ni(OH)_2$ and the corresponding elemental mapping images of O, Ni and Zr.

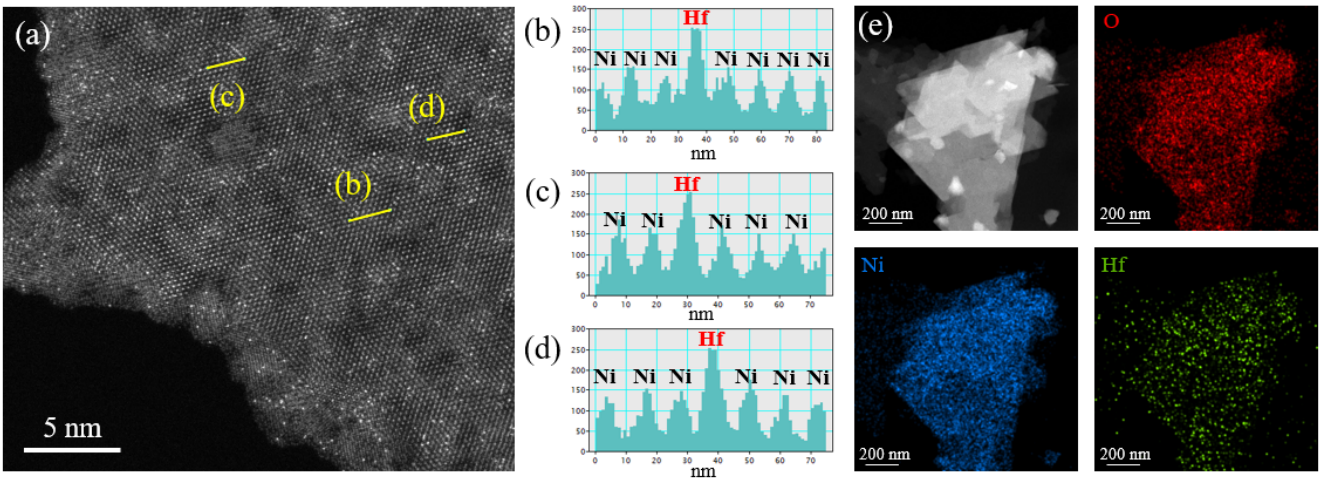

Fig. S13. (a) HAADF-STEM image of $Hf_1/Ni(OH)_2$ and (b-d) the corresponding brightness intensity of the yellow line profiles taken in the HAADF-STEM image. (e) HAADF-STEM image of $Hf_1/Ni(OH)_2$ and the corresponding elemental mapping images of O, Ni and Hf.

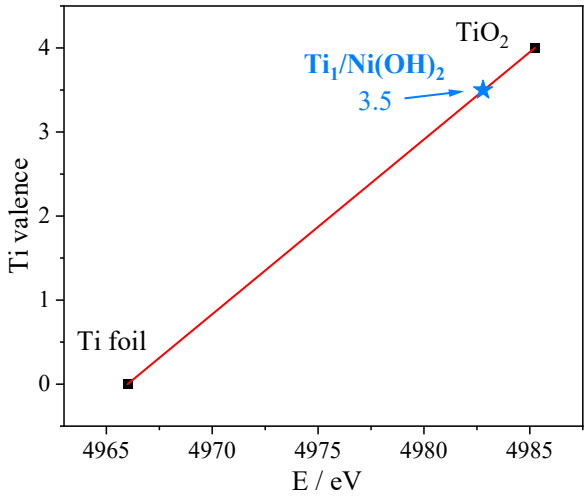

Fig. S14. Fitted average oxidation states of Ti in Ti foil, TiO_2 and $Ti_1/Ni(OH)_2$.

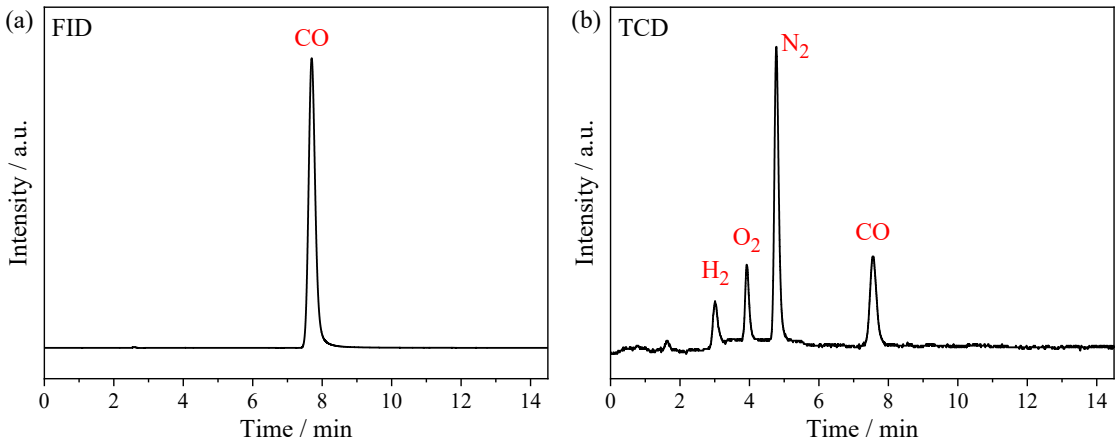

Fig. S15. GC profiles for the gaseous products from the photocatalytic experiments of $Ti_1/Ni(OH)_2$.

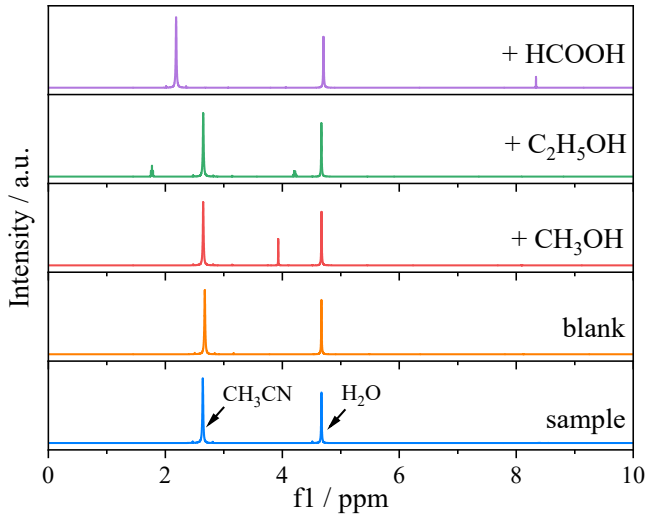

Fig. S16. ^1H NMR spectra of the liquid products from the photocatalytic experiments of $Ti_1/Ni(OH)_2$. Deuterated solvent: D_2O.

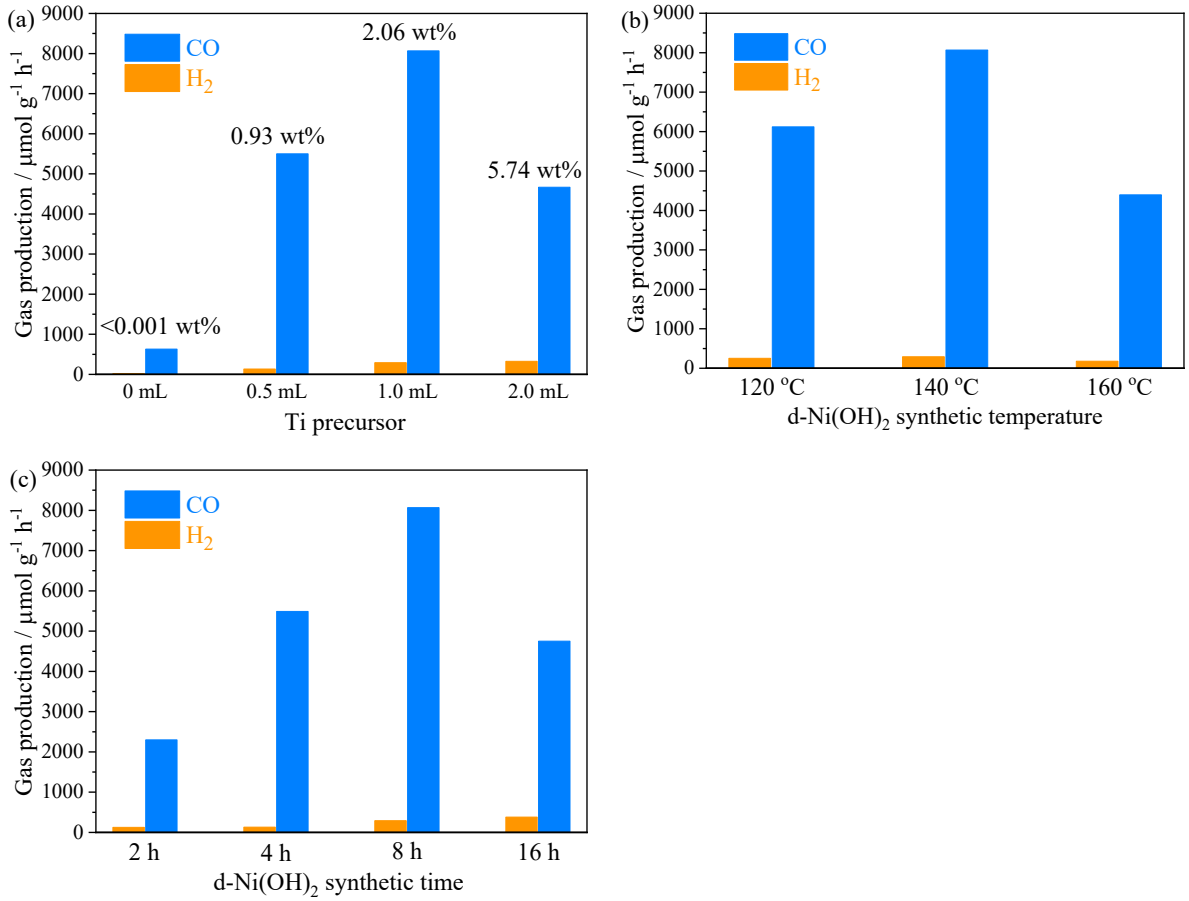

Fig. S17. Performance of photocatalytic CO_2 reduction using $Ti_1/Ni(OH)_2$ prepared under different conditions: (a) different amounts of Ti precursor/Ti wt%, (b) different synthetic temperatures and (c) synthetic times of d-$Ni(OH)_2$

Shorter time or lower temperature in d-$Ni(OH)_2$ synthesis may lead to less defective support, which cause the lack of anchoring sites for monodispersed Ti atoms, resulting in inadequate active sites and lower performance. On the other hand, longer time or higher tempareture in d-$Ni(OH)_2$ synthesis may cause complete collapse of support, hindering charge transfer in photocatalysis and leading to lower performance. As for the amount of Ti precursor, which directly affects the Ti content of Ti/$Ni(OH)_2$, lower amount leads to insufficient active sites, while higher amount could lead to aggregation and stacking of neighboring active sites or even partially destroyed support, both of which have negative effects on photocatalytic performance.

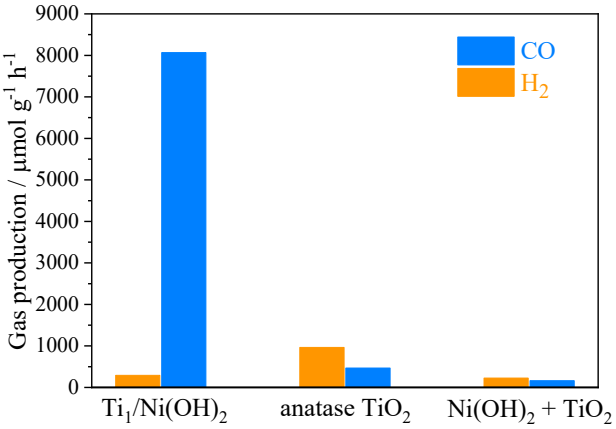

Fig. S18. Comparison of the photocatalytic performances of $Ti_1/Ni(OH)_2$, anatase TiO_2 and the mixture of $Ni(OH)_2$ + TiO_2.

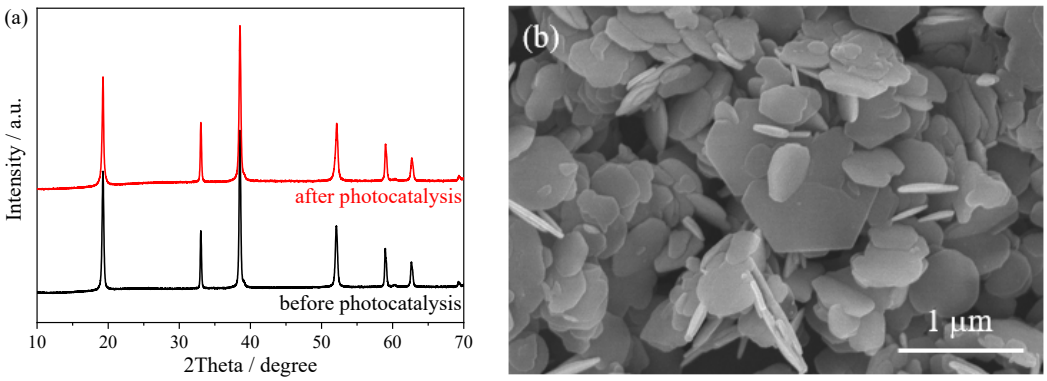

Fig. S19. Stability test of $Ti_1/Ni(OH)_2$ after photocatalytic experiments. (a) PXRD patterns, (b) SEM image.

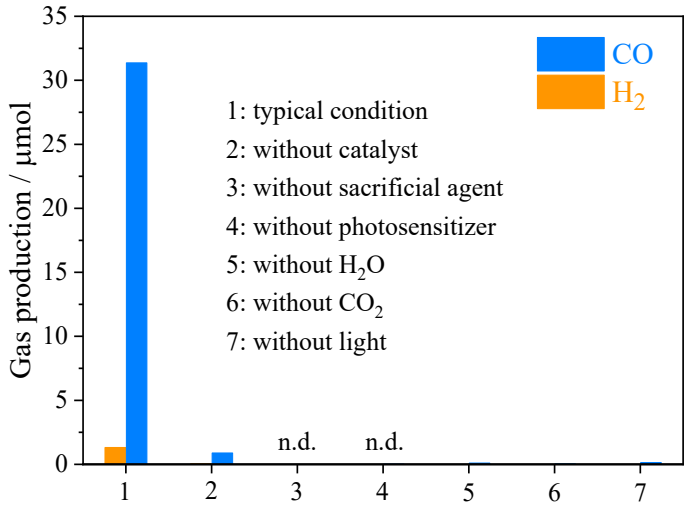

Fig. S20. Control experiments of catalytic conditions.

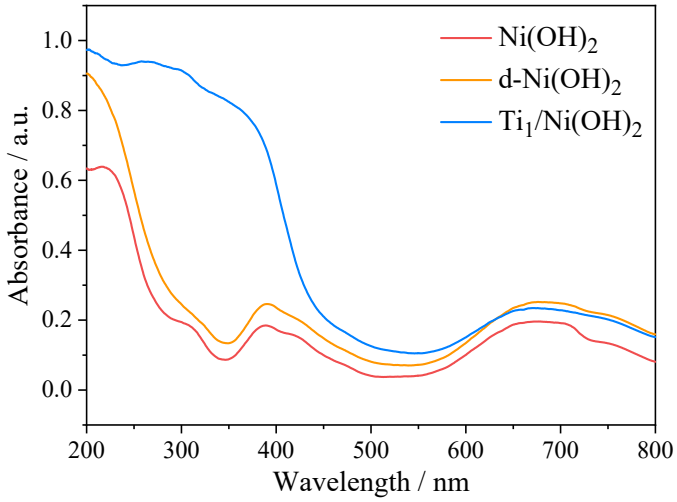

Fig. S21. UV-vis spectra of $Ti_1/Ni(OH)_2$, d-$Ni(OH)_2$ and $Ni(OH)_2$.

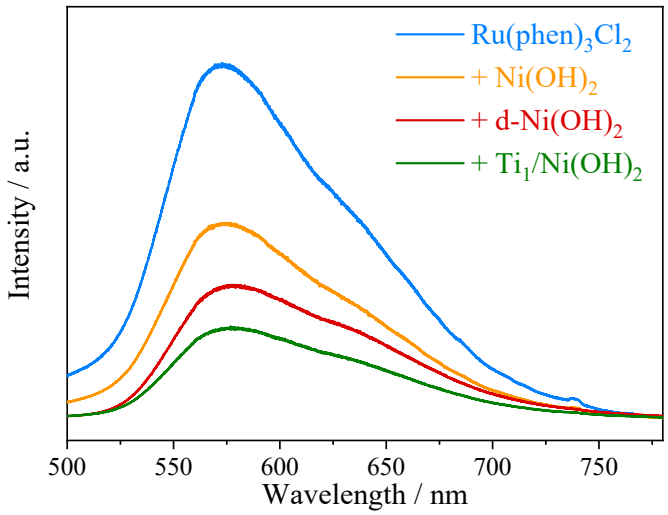

Fig. S22. PL emission spectra of $[Ru(phen)_3]Cl_2 \cdot 6H_2O$ with the colloidal suspension of $Ni(OH)_2$, d-$Ni(OH)_2$ and $Ti_1/Ni(OH)_2$ excited with 465 nm light.

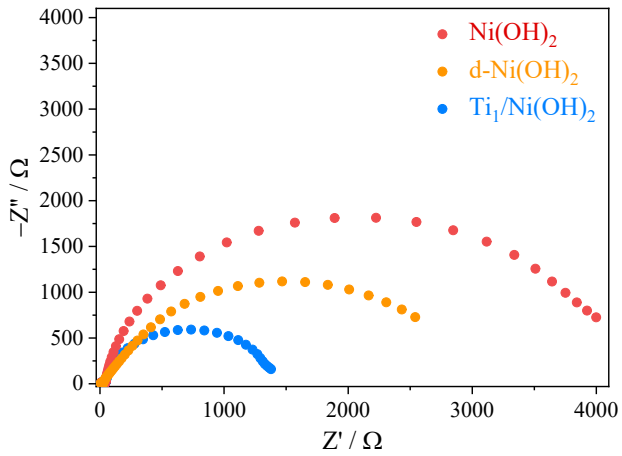

Fig. S23. EIS Nyquist plots of $Ni(OH)_2$, d-$Ni(OH)_2$ and $Ti_1/Ni(OH)_2$.

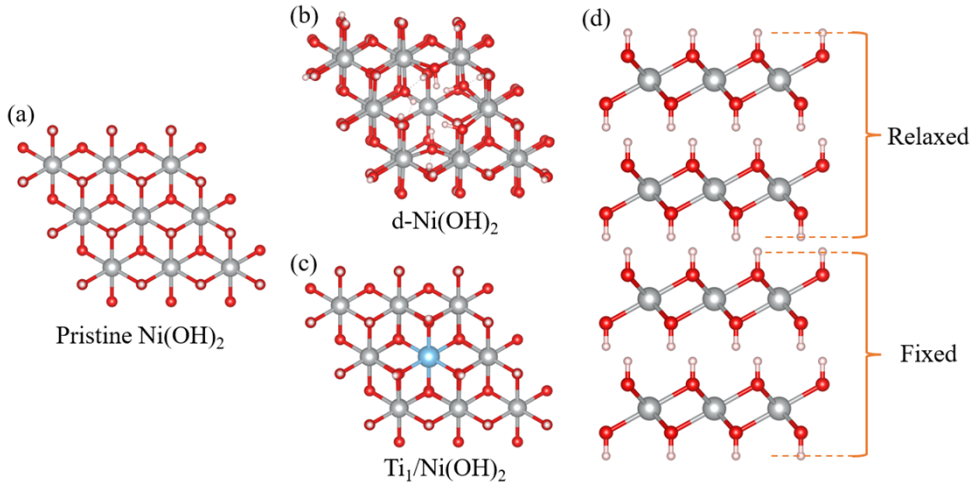

Fig. S24. Atomic structures of (a) $Ni(OH)_2$, (b) d-$Ni(OH)_2$ and (c) $Ti_1/Ni(OH)_2$. Color codes: red, O; gray, Ni; cyan, Ti; white, H.

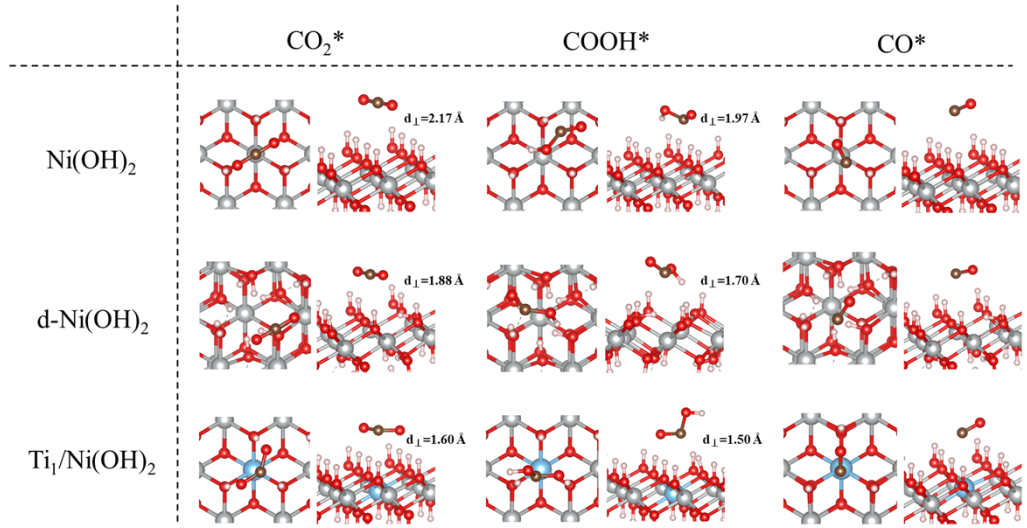

Fig. S25. Adsorption configurations of intermediates involved in photocatalytic CO_2 reduction on $Ni(OH)_2$, d-$Ni(OH)_2$ and $Ti_1/Ni(OH)_2$. Distances ($d_\perp$) represent the vertical distance between substrates and reaction intermediates (CO_2* and COOH*). Color codes: red, O; gray, Ni; cyan, Ti; brown, C; white, H.

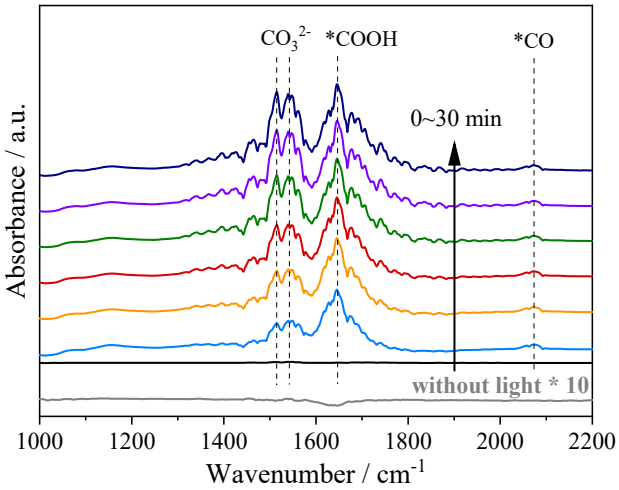

Fig. S26. In-situ FTIR spectra of the photocatalytic CO_2 reduction on $Ti_1/Ni(OH)_2$.

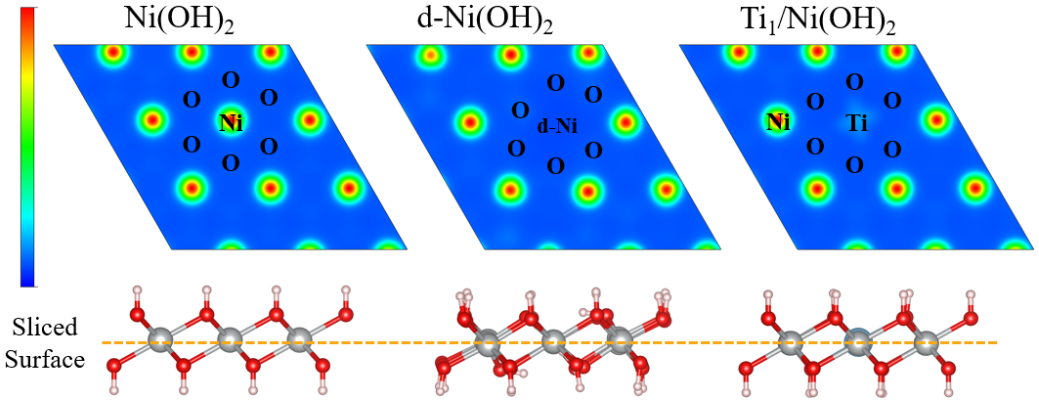

Fig. S27. Charge density distribution of $Ni(OH)_2$, d-$Ni(OH)_2$ and $Ti_1/Ni(OH)_2$.

Table S1. ICP-MS analysis results of $Ti_1/Ni(OH)_2$.

$Ti_1/Ni(OH)_2$	w_{Ni}/mg L^{-1}	w_{Ti}/mg L^{-1}	n_{Ni}/mmol L^{-1}	n_{Ti}/mmol L^{-1}	Ti wt%
Test 1	63.1	1.98	1.07	0.041	1.99
Test 2	40.4	1.41	0.69	0.029	2.21
Test 3	40.7	1.27	0.69	0.026	1.98
average	/	/	/	/	2.06
Mother liquor from d-$Ni(OH)_2$ synthesis	8.36	/	0.14	/	1.86% of Ni dissolved[a]
$Ti_1/Ni(OH)_2$ before photocatalysis	41.6	1.41	0.71	0.029	2.14
$Ti_1/Ni(OH)_2$ after photocatalysis	115.6	3.81	1.96	0.079	2.09
Mother liquor from photocatalysis	0.011	0.0013	/	/	0.13% of Ni and 0.32% of Ti dissolved
0 mL Ti precursor	186.5	0.0055	3.16	0.00011	<0.001
0.5 mL Ti precursor	183.3	2.67	3.11	0.056	0.93
2.0 mL Ti precursor	53.9	4.87	0.91	0.10	5.74

[a]As presented in the experimental details, d-$Ni(OH)_2$ was synthesized from 50 mg $Ni(OH)_2$ in a mixed solution with a total volume of 7 mL. Prior to the ICP-MS tests, only 1 mL of the mother liquor was used for digestion and eventually diluted to 10 mL. According to the ICP-MS result, the concentration of Ni ions in the digestion solution was detected as 8.36 mg L^{-1}. The mass fraction of Ni in $Ni(OH)_2$ is 63.3%. Therefore, the percentage of leaking Ni was calculated as: (8.36 mg L^{-1} × 10 mL × 0.001 × 7) / (50 mg × 63.3%) × 100% = 1.86%, which confirmed that most of the introduced Ti atoms were anchored in the defect sites.

Table S2. EXAFS fitting parameters at the Ti K-edge for various samples

Sample	Shell	CN^a	R(Å)^b	σ^2(Å^2)^c	ΔE_0(eV)^d	R factor
TiO_2	Ti-O	6	1.94±0.01	0.0047±0.0010	-5.0±1.5	0.0120
Ti foil	Ti-Ti	6	2.91±0.02	0.0062±0.0004	5.0±0.8	0.0175
$Ti_1/Ni(OH)_2$	Ti-O	5.7	2.02±0.10	0.0092±0.0011	-1.4±2.1	0.0115

[a]*CN*, coordination number;

[b]*R*, distance between absorber and backscatter atoms;

[c]σ^2, Debye-Waller factor to account for both thermal and structural disorders;

[d]ΔE_0, inner potential correction;

[e]*R* factor indicates the goodness of the fit.

S_0^2 was fixed to 0.7, according to the experimental EXAFS fit of Ti foil by fixing *CN* as the known crystallographic value. Fitting range: $3.0 \leq k$ (/Å) ≤ 12 and $1.0 \leq R$ (Å) ≤ 2.0 (TiO_2); $3.0 \leq k$ (/Å) ≤ 12.0 and $1.0 \leq R$ (Å) ≤ 3.0 (Ti foil); $3.0 \leq k$ (/Å) ≤ 12.0 and $1.0 \leq R$ (Å) ≤ 2.0 ($Ti_1/Ni(OH)_2$).

Table S3 Comparison of the photocatalytic activities of $Ti_1/Ni(OH)_2$ and other reported catalysts for photocatalytic CO_2 reduction to CO.

Material	Solvent	λ	Major Products	Generation Rate / mmol g^{-1} h^{-1}	CO Selectivity	Ref.
$Ti_1/Ni(OH)_2$	CH_3CN-H_2O	410–760 nm	CO, H_2	CO 8.09	96.5%	**This work**
Co-OAc	CH_3CN	>380 nm	CO, H_2	CO 2.33	99.1%	*J. Am. Chem. Soc.* **2024**, *146*, 3241
$Zn_xCd_{1-x}S$−Co_1	CH_3CN-H_2O	>400 nm	CO, H_2	CO 7.63	/	*J. Am. Chem. Soc.* **2024**, *146*, 9721
Ni-SA	CH_3CN-H_2O	410–760 nm	CO, H_2	CO 6.96	96.6%	*Nano Res.* **2023**, *16*, 7756
Co-SA	CH_3CN-H_2O	410–760 nm	CO, H_2	CO 2.95	73.8%	
NNU-55-Ni	CH_3CN-H_2O	≥ 420 nm	CO, H_2	CO 0.267	81.0%	*Nat. Comm.* **2022**, *13*, 2964.
HOF-25-Ni	CH_3CN-H_2O	> 420 nm	CO, H_2	CO 20.7	86.5%	*Angew. Chem. Int. Ed.* **2022**, *61*, e202211482.
BIF-107	CH_3CN-H_2O	> 420 nm	CO, H_2	CO 1.19	55.7%	*Inorg. Chem.* **2020**, *59*, 17851.
2D-Co_2TCPE	CH_3CN-H_2O	> 420 nm	CO, H_2	CO 4.15	74.36%	*Angew. Chem. Int. Ed*. **2020**, *59*, 23588.
2D-Ni_2TCPE	CH_3CN-H_2O	> 420 nm	CO, H_2	CO 3.00	97.3%	
PCN-250-Fe_2Mn	CH_3CN-H_2O	> 420 nm	CO, H_2	CO 21.51	82.17%	*Appl. Catal. B: Environ.,* **2020**, *276,* 119173.
MAF-X27*l*-OH	CH_3CN-H_2O	420 nm	CO, H_2	/	98.2%	*J. Am. Chem. Soc.* **2018**, *140*, 38.
MOF-525-Co	CH_3CN	> 400 nm	CO、CH_4	CO 0.20	84.6%	*Angew. Chem. Int. Ed*. **2016**, *55*, 14310.
Ni MOLs	CH_3CN-H_2O	> 400 nm	CO、H_2	CO 12.5	97.8%	*Angew. Chem. Int. Ed*. **2018**, *57*, 1.

References

1 D. S. He, *Ultramicroscopy*, 2023, **253**: 113797.

2 T.-H. Wu, B.-W. Hou, *Catal. Sci. Technol.*, 2021, **11**, 4294.

3 P. E. Blöchl, *Phys. Rev. B,* 1994, **50**, 17953-17979.

4 (a) G. Kresse, J. Furthmüller, *Phys. Rev. B* 1996**, 54**, 11169-11186; (b) G. Kresse, J. Furthmüller, *Comp. Mater. Sci.* 1996**, 6**, 15-50.

5 J. P. Perdew, K. Burke, M. Ernzerhof, *Phys. Rev. Lett.* 1996**, 77**, 3865-3868.

6 (a) Y. Sakamoto, Y. Noda, K. Ohno, S. Nakamura, *J. Phys. Chem. C* 2017**, 121**, 24603-24611; (b) S. J. Johnston, R. M. Choueiri, X. Liu, B. J. R. Laframboise, S. W. Tatarchuk, L. D. Chen, *J. Phys. Chem. C* 2024**, 128**, 5568-5578; (c) A. Tilocca, A. Selloni, *J. Phys. Chem. C* 2012**, 116**, 9114-9121; (d) A. Alghannam, C. L. Muhich, C. B. Musgrave, *Phys. Chem. Chem. Phys.* 2017**, 19**, 4541-4552.

7 J. K. Nørskov, J. Rossmeisl, A. Logadottir, L. Lindqvist, J. R. Kitchin, T. Bligaard, H. Jónsson, *J. Phys. Chem. B* 2004**, 108**, 17886-17892.